A spectral study of the Caloris basin on Mercury and the origin of associated volcanic smooth plains

E. Caminiti, A. Doressoundiram, S. Besse, J. Wright

A spectral study of the Caloris basin on Mercury and the origin of associated volcanic smooth plains

E. Caminiti[1], A. Doressoundiram[1], S.Besse[2], J.Wright[2]

[1]LESIA, Observatoire de Paris, Université PSL, CNRS, Sorbonne Université, Université de Paris, 5 place Jules Janssen, 92195 Meudon, France
[2] European Space Agency (ESA), European Space Astronomy Centre (ESAC), Camino Bajo del Castillo s/n, 28692 Villanueva de la Cañada, Madrid, Spain

Corresponding author: E.Caminiti, emma.caminiti@obspm.fr

Key points

- The exterior volcanic plains of Caloris were emplaced in and around the basin followed by the interior plains within the basin only.
- The melting degree and/or melting depth decrease over time between the formation of the exterior and interior plains.
- Spectral and compositional data show heterogeneous exterior plains with an east-west asymmetry.

Abstract

Results from the NASA/MESSENGER mission showed that 27% of Mercury's surface is covered by smooth plains mostly produced by extensive effusive volcanism. The Caloris impact basin is associated with two, mostly volcanic, smooth plains, one in its interior and one surrounding the basin. Previous studies have shown that it is difficult to estimate the relative ages of the interior and exterior plains and to explain their spectral and compositional differences. We perform an exhaustive spectral analysis of the basin based on data obtained by the MASCS spectrometer onboard MESSENGER between 300 and 1450 nm with a 5 nm resolution. Unlike previous results based on crater counts, we found that the exterior plains were emplaced before the interior plains although both postdate the formation of the basin. We propose a decrease in the partial melting degree and/or partial melting depth over time to explain the spectral and compositional differences. The study highlights spectrally heterogeneous exterior plains associated with a compositional heterogeneity and the presence of Low Reflectance Material deposits. This heterogeneity in the exterior plains could be related to the formation of the basin and an asymmetry of the ejecta deposits or to a heterogeneous distribution of Low Reflectance Material present at depths before the formation of the basin.

Plain Language Summary

Results from the NASA/MESSENGER mission highlighted several geological units at the surface of Mercury. The volcanic plains are defined as a sparsely cratered unit with several embayment of other landforms. Most of these plains formed by effusive volcanism before 3.5 Ga. Caloris, the largest well-preserved impact basin is associated with two plains, mostly volcanic, one filling the basin and one surrounding the basin, which have different spectral and compositional properties. Previous studies have shown that it is difficult to estimate the relative ages of the interior and exterior plains. In this work we perform an exhaustive spectral analysis of Caloris based on MESSENGER data. Unlike previous results we found that the exterior plains are older and were emplaced before the interior plains although both postdate Caloris formation. We propose an evolution of the volcanic source conditions over time to explain the spectral and compositional differences between the exterior and interior plains. A decrease in the partial melting degree and/or partial melting depth over time lead to modifications of magma properties and different compositional and spectral properties of lava. This study highlights heterogeneous exterior plains with an east-west asymmetry.

1 Introduction

The study of geological processes such as impact cratering and volcanism provides information on the evolution of Mercury since its formation (Marchi et al., 2013; Byrne., 2020). Impact basins (Osinski et al., 2022) have a significant role in modifying the surface, notably through the redistribution of material and modification of geological units (Fassett et al., 2012; Kincyk et al., 2020). In addition, they expose vertical heterogeneities in the crust and allow to reconstruct the subsurface stratigraphy (Ernst et al., 2010; D'Incecco et al., 2015; 2016). Volcanism has molded Mercury's surface and considerably modified impact basins after their formation by the emplacement of younger volcanic layers (Denevi et al., 2009; Marchi et al., 2011; Wang et al., 2021; Wright et al., 2021).

As the origin of spectral differences on Mercury is not fully understood, it is difficult to conclude about their origin (composition, grain sizes, space weathering). Here, we propose a new method using Mercury Atmospheric and Surface Composition Spectrometer (MASCS) (McClintock & Lankton., 2007) data from the MErcury Surface, Space ENvironment, GEochemistry, and Ranging (MESSENGER) mission (McNutt et al., 2006; Solomon et al., 2007) to provide more information on the relative timing of the formation of the interior and exterior volcanic smooth plains associated with the Caloris basin. We will focus on the spectral and compositional differences between the two plains and the evolution of magmatism through time to reconstruct the history of the basin's evolution. This spectral investigation of the Caloris basin allows the study of the subjacent stratigraphy as well as a better understanding of deep melting processes.

2 Smooth plains and spectral properties of Mercury after MESSENGER

Observations by Mariner 10 revealed relatively young smooth plains on the surface of Mercury, the nature of which remained uncertain between a volcanic origin (Strom et al., 1975; Kiefer & Murray., 1987; Spudis & Guest, 1988) or impact-origin plains in the form of fluidized ejecta (Wilhelms et al., 1976; Oberbeck et al., 1977). It was with the observations of the MESSENGER mission that volcanic indicators could be confirmed, 27% of Mercury's surface is covered by smooth plains, with more than 65% produced by an extensive effusive volcanism before 3.5 Ga (Head et al., 2008, 2009, 2011; Denevi et al., 2013; Marchi et al., 2013; Byrne et al., 2016, Wang et al., 2021). The distribution of smooth plains is asymmetric with more smooth plains located in the northern hemisphere. They are also mainly concentrated inside and/or around major impact basins. The 3 most significant smooth plains are Borealis Planitia (9% of the surface) (Head et al., 2011), the interior (2% of the surface) and exterior plains (7% of

the surface) of the Caloris basin (Ernst et al., 2015; Fassett et al., 2009). Caloris is the largest well-preserved impact basin on Mercury with a diameter of 1,550 km (Murchie et al., 2008). In the following, we will refer to Caloris' smooth plains as the " exterior plains " and the " interior plains ". Moreover, in this work HRP will be associated with Caloris interior plains without taking into account HRP elsewhere on the planet. Although small patches are still debated (Wang et al., 2021), both the interior and exterior plains are mostly volcanic in origin (Rothery et al., 2017; Wright et al., 2021).

Results from the MESSENGER mission have identified different spectral color units (Robinson et al., 2008; Denevi et al., 2009; Ernst et al., 2010; Murchie et al., 2015) that are not systematically associated with geological units (Murray et al., 1975; Trask and Guest., 1975; Spudis and Guest., 1988; Denevi et al., 2013) or compositional units (Peplowski et al., 2015; Weider et al., 2015; Nittler et al., 2020; Vander Kaaden et al., 2017; Namur & Charlier, 2017). Among the numerous spectral color units (see Table 1 of Murchie et al., 2015 and D'Incecco et al., 2015) are: fresh crater materials characterized by brighter reflectance and slightly bluer spectral slopes than the average (Ernst et al., 2010), bright hollow materials showing in a significant way a higher reflectance and bluer slopes than surroundings (Blewett et al., 2013; Barraud et al., 2020), the red unit interpreted as pyroclastic vents with a relatively red spectra and high reflectance (Robinson et al., 2008; Ernst et al., 2010; Barraud et al., 2021), intermediate plains (Denevi et al., 2009), high-reflectance red plains (HRP), low-reflectance blue plains (LBP) and low reflectance material (LRM). HRP have a steeper reflectance spectrum slope in the visible to near-infrared domain than the planet's average and a high reflectance at 750 nm (20% higher than the global average). Most of the smooth plains, including the interior of Caloris, are spectrally classified as HRP. The exterior smooth plains of Caloris have a lower reflectance, a lower spectral slope than the planet's average and belong to the LBP (Robinson et al., 2008; Denevi et al., 2009; Murchie et al., 2015) (Figure1). Nonetheless, the HRP and LBP are not sufficient to cover the spectral diversity of the Caloris basin and associated smooth plains (Robinson et al., 2008; Ernst et al., 2010, 2015). Indeed, the formation of impact basins/craters brings deep material to the surface (Murchie et al., 2015; D'Incecco et al., 2015; Klima et al., 2018). Some of the excavated material has a low reflectance (30% below the global mean), a low spectral slope (5% lower than HRP) and is classified as LRM. LRM deposits are hypothesized to be exhumed remnants of Mercury's putatively carbon-rich primary crust buried under the secondary volcanic crust (Denevi et al., 2009; Vander Kaaden & McCubbin, 2015; Peplowski et al., 2016; Klima et al., 2018). LRM is mostly exposed in impact crater materials (crater walls, floors, central uplifts, and rims), such as Rachmaninoff, Tolstoj and Bashō (Robinson et al., 2008; Klima et al., 2018) (Figure 1). Several craters in the Caloris basin's interior plains have LRM in their ejecta or interior, providing evidence of LRM beneath Caloris (Ernst et al., 2010; Ernst et al., 2015). In total, 15% of Mercury's surface is covered by LRM highlighting the importance of this spectral unit for the study of Mercury's evolution (Denevi et al., 2009).

In addition to their spectral differences, results obtained with the MESSENGER/X-ray Spectrometer (XRS) and Gamma-Ray Spectrometer (GRS) highlighted different

compositions between the interior and exterior plains (Denevi et al., 2013; Weider et al., 2015; Vander Kaaden et al., 2017; Nittler et al., 2020). The exterior plains are composed of a more ultramafic lava, richer in Mg and poorer in Al than the interior plains.
Both the interior and exterior plains associated with the Caloris basin were emplaced after the basin's formation, recently estimated to have occurred around 3.94 +- 0.04 Gyr (Hirata et al., 2022). Both plains were emplaced within a short span of time, which makes relative dating by impact crater counting difficult as the error bars overlap. The exterior plains of the Caloris basin appear to be contemporary with the formation of the Northern Smooth Plains (NSP) around 3.7 Gyr ago, when the largest smooth plains were emplaced on Mercury (Denevi et al., 2013; Wright et al., 2021). Thereafter, volcanism would have become less voluminous, occurring in patches and within impact basins (Marchi et al., 2013). However, some studies show that the exterior plains could be slightly younger than the interior plains for Caloris, but there is a significant margin of error and the relative timing remains controversial (Strom et al., 2008 2011; Fassett et al., 2009; Head et al., 2011; Denevi et al., 2013; Rothery et al., 2017).

3 Materials and Method

- 3.1 Dataset and spectral parameters

- 3.1.1 MESSENGER/MASCS data

In this study we use spectral data obtained by the Visible and Infrared Spectrograph (VIRS) of the MASCS instrument (McClintock & Lankton., 2007) onboard MESSENGER. We used radiometrically and photometrically corrected data available on the Planetary Data System (PDS). VIRS is composed of two detectors allowing the study of the surface of Mercury with a 5 nm spectral resolution from the visible (VIS) to the near-infrared (NIR) thanks to corrections developed by Besse et al., 2015. The correction consists of smoothing the spectrum and correcting the offset between the visible (VIS) and near-infrared (NIR) detectors giving a full spectrum between 300 and 1450 nm with a 5 nm spectral resolution. The corrected spectra (Besse et al., 2015), the original publicly available metadata from the archives (including data quality and geometry of observation) and a set of spectral parameters are now organized in a relational database. The database contains 4.7 million observations and is known as the Mercury Surface and Spectroscopy (MeSS) database (Besse et al., 2022; Cornet et al., 2022).

- 3.1.2 Data filtering

The instrumental temperature and/or observation conditions can bias the measurements and need to be controlled and properly filtered (Izenberg et al., 2014). The detectors, and particularly the NIR detector, are sensitive to the instrumental temperature that can reduce the signal-to-noise ratio. The MESSENGER team indexed MASCS data according to the instrument temperature (<15°C, <25°C, <40°C and ≥40°C) at the time of the measurement. To maximize the amount of data available for analysis, while ensuring data quality, we filtered out all data recorded with a temperature ≥40°C. Shadows, which become increasingly pervasive as the solar incidence angle increases, reduce the quality of MASCS spectra; consequently, data with an incidence angle above 75° were removed. Elongated MASCS footprints may overlap several spectral color units, thus only footprints with an area smaller than 65 km^2 were analyzed. The filters remove 24% (i.e, 1.1 million spectra) of the data initially available (i.e, 4.7 million spectra) mainly at high latitudes and the hot poles. These hot poles are due to the resonance of the 3:2 spin orbit: local noon at longitudes 0° W and 180° W corresponds to perihelion, while longitudes 90◦ W and 270◦ W have local noon at aphelion, which gives rise to 'hot' and 'warm' poles around the equator (Bauch et al., 2021). Above hot poles the instrumental temperature is higher due to the orbital position as well as the flux received from the surface giving rise to many data obtained with an instrumental temperature above 40°C.

- 3.1.3 Parameters highlighting spectral units

A large number of spectral parameters can be used for the analysis of Mercury's surface and have already led to numerous results, notably concerning pyroclastic deposits and hollows (Goudge et al., 2014; Besse et al., 2015; Bott et al., 2019; Besse et al., 2020; Barraud et al., 2020, 2021, Zambon et al., 2022). In this study, we selected spectral parameters that, individually or in combination with each other, effectively distinguish the interior Caloris plains (HRP), the exterior Caloris plains (LBP) and the LRM (Table 1).

Spectral parameters	Spectral range (nm)	Mathematical expression	Description
VIS-Slope	445 - 750	$Reflectance(\lambda) = VIS_{Slope} \times \lambda + b$	Slope in the visible part of the spectrum. Obtained by a linear fit.
R750	745 - 755	$R(750nm)$	The reflectance at 750 nm is an average value of 3 points due to the smoothing correction method using a moving average window of 3 points (Besse et al

			2015).
UV-Downturn	300 - 400	*Depth300+Depth325+Depth350* *With :* $Depth300 = \frac{R401 - (401 - 303) * VIS_{Slope}}{R303}$ $Depth325 = \frac{R401 - (401 - 324) * VIS_{Slope}}{R324}$ $Depth350 = \frac{R401 - (401 - 350) * VIS_{Slope}}{R350}$ $VIS_{Slope} = \frac{R550 - R750}{550 - 750}$	Drop of the reflectance in the UV. Offset between measured reflectances and expected reflectances (Goudge et al., 2014).
VISNIR-Slope	445 - 1400	$R(\lambda) = VISNIR_{Slope} \times \lambda + b$	Slope in the visible to nir-infrared part of the spectrum. VIS-Slope extended to 1400 nm by a linear fit.
Color index 415/750	415 - 750	$\frac{R415}{R750}$	Reflectances ratio

Table 1: Spectral parameters allowing the study of units related to the Caloris impact basin.

3.2 Statistical analysis and spectral units' properties

- 3.2.1 Sampling of spectral units

In order to obtain the spectral properties associated with the LRM, LBP and HRP units with MASCS data and better understand the origin and relative timing of interior and exterior volcanic plains of Caloris, several areas were sampled (Figure 1). A total of 30 areas were selected, 15 located on the interior plains (HRP) and 15 on the exterior plains (LBP). The aim was to obtain a sampled area large enough to best represent the units of interest. The sampled areas were selected avoiding topographic perturbations (craters, wrinkle ridges), other spectral units (fresh material) and areas where spatial coverage is insufficient with MASCS. In total, an area of 429,000 km^2 separated into 2×15 areas of 214,879 km^2 for the interior plains and 214,121 km^2 for the exterior plains were sampled.
The LRM was sampled with the same precautions around different basins known to have deposits containing different amounts of carbon: Atget, Tolstoj, Bashō and Rachmaninoff (Peplowski et al., 2016; Klima et al., 2018).

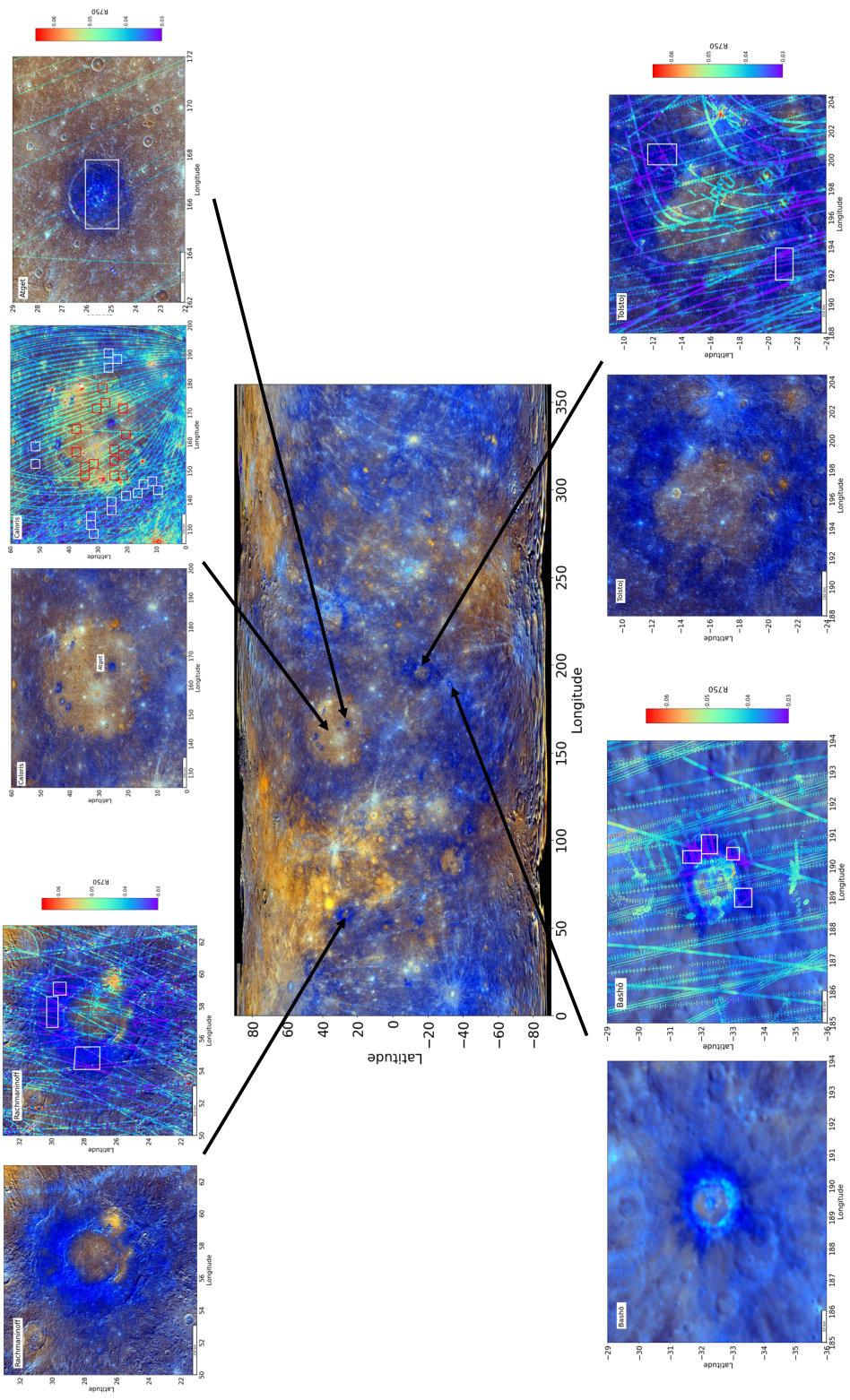

Figure 1: Global MDIS enhanced color map with the location of sampled areas. For each location are shown MDIS enhanced color map and a map of MASCS footprints. White boxes on Rachmaninoff, Bashō, Tolstoj and Atget represents the sampling of LRM. Concerning Caloris, red and white boxes show respectively the sampling of the interior HRP and the exterior LBP.

- 3.2.2 Spectral units' properties using MASCS data

A statistical analysis was applied to the sampled MASCS footprints for the spectral units, LRM, LBP and HRP, in order to obtain the properties of each unit for the four spectral parameters: R750, VIS_Slope, UV_Downturn and VISNIS_Slope (Table 1). The mean and standard deviation were calculated for each unit and each parameter to define a unit-specific framework (Table 2). The framework consists of the mean and the standard deviation giving a range of values associated with each parameter and each spectral unit (Table 1). The 415/750 ratio will not be used for the study of the interior and exterior plains as it does not allow the distinction between them (Figure 3). However, it will be introduced to specify the spectral properties of the LRM (see 3.3).

Two confidence levels were established (Table 2). In the first level (L1) the framework is based on 100% of the sampled data remaining after the filters in temperature, incidence angle and footprint size (see section 3.1.2). The mean and standard deviation were calculated for each unit and each spectral parameter giving a framework for each of them. If there is an overlap of frameworks between units for the same spectral parameter, the overlap range is cropped to avoid ambiguity and to obtain a clear separation between each unit for every parameter. For example: the reflectance at 750 nm does not allow an unambiguous distinction between LRM and LBP. The LRM full range is $0.026466<R750<0.033158$ and the LBP full range is $0.031045<R750<0.040658$. There is a range between 0.031045 and 0.033158 where it will not be possible to classify the footprint between LBP or LRM. In order to remove this ambiguity, we reversed the boundaries and cut the frameworks to mark this area of overlap as an area where it is not possible to distinguish the two units. The boundaries become: $0.026466 \leq R750 < 0.031045$ for the LRM and $0.033158 < R750 \leq 0.040658$ for the LBP (Table 2).

The second level (L2) (Table 2), which is more selective, was obtained using 50% of the data closest to the mean including data between the first and third quartile. The mean and standard deviation were calculated within this new set of data in order to obtain in the same way as L1 more restricted frameworks avoiding extreme values. This approach, using only the data closest to the mean, avoids any overlap between units giving greater confidence in these frameworks. The L2 level allows a better distinction between units than L1 as none of the framework has to be cropped to clearly separate units with all the spectral parameters.

Spectral units Spectral parameters	Low Reflectance Material	Low-reflectance Blue Plains	High-reflectance Red Plains
Level 1 (L1): 100% of the sampled data			
R750	$0.026466 \leq R750 < 0.031045$ *	$0.033158 < R750 \leq 0.040658$ *	$0.041653 \leq R750 \leq 0.049259$
VIS_Slope	$0.45598 \leq VIS_{Slope} \leq 0.59218$	$0.62511 \leq VIS_{Slope} \leq 0.81237$	$0.87746 \leq VIS_{Slope} \leq 1.0143$
UV_Downturn	$2.9332 \leq UV_{Downturn} < 2.9825$ *	$3.0850 < UV_{Downturn} < 3.1521$ *	$3.1998 < UV_{Downturn} \leq 3.2651$*
VISNIR_Slope	$0.47392 \leq VISNIR_{Slope} < 0.62076$ *	$0.74192 < VISNIR_{Slope} < 0.93362$ *	$0.96964 < VISNIR_{Slope} \leq 1.1712$ *
Level 2 (L2): 50% of the sampled data			
R750	$0.028689 \leq R750 \leq 0.030277$	$0.034824 \leq R750 \leq 0.037080$	$0.043668 \leq R750 \leq 0.046574$
VIS_Slope	$0.50698 \leq VIS_{Slope} \leq 0.54916$	$0.70090 \leq VIS_{Slope} \leq 0.75328$	$0.91394 \leq VIS_{Slope} \leq 0.97022$
UV_Downturn	$2.9963 \leq UV_{Downturn} \leq 3.0489$	$3.0708 \leq UV_{Downturn} \leq 3.1234$	$3.1900 \leq UV_{Downturn} \leq 3.2288$
VISNIR_Slope	$0.56310 \leq VISNIR_{Slope} \leq 0.64429$	$0.74745 \leq VISNIR_{Slope} \leq 0.85841$	$1.0188 \leq VISNIR_{Slope} \leq 1.0928$

*Table 2: Frameworks obtained from the statistical analysis of the sampled areas for the study of LRM, LBP and HRP using four spectral parameters. Two confidence levels are studied each using 100% (L1) and 50% (L2) of the sampled data. Frames identified by a * were cropped because of an overlap between spectral units to avoid any ambiguity concerning the spectral distinction of units.*

3.3 Distinction of units according to spectral parameters

In order to be able to identify LRM, LBP and HRP with MASCS it is important to take into account the different capabilities of the spectral parameters used to discriminate the three units (Figure 2). With the aim of giving more importance to the spectral parameters that most clearly distinguish one unit from another a quality parameter has been created where the maximum mark is 16 points (Table 3). The properties of each footprint around Caloris are analyzed in order to associate it or not with one of the units according to the quality parameter.

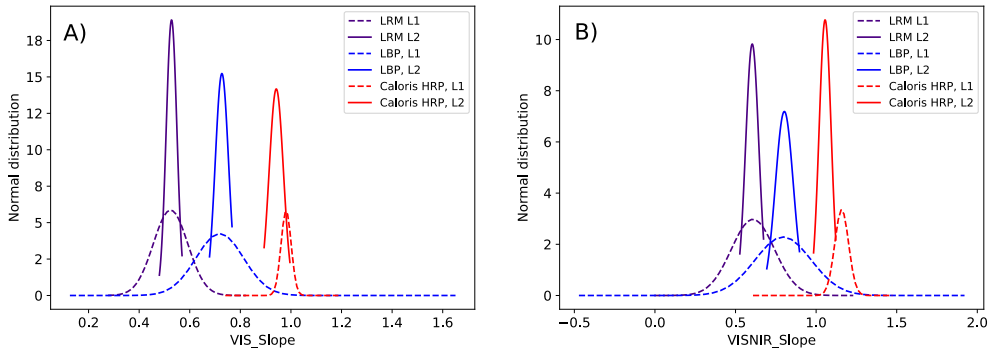

Figure 2: Normal distribution of sampled data highlighting the capability of the VIS_Slope and the VISNIR_Slope parameters to separate the three spectral units. A) The VIS_Slope parameter allows a good discrimination of units according to L1 and L2. B) By comparison, the VISNIR_Slope parameter shows a significant overlapping of units concerning L1.

For frameworks obtained with L2 (Table 2) each of the parameters is able to distinguish the three spectral units without the need to crop any framework. The same importance is attributed to each of these parameters concerning their capacity to distinguish LRM, LBP and HRP. The weight assigned to a footprint having one of the properties inside L2 is four (Table 3).
Regarding frameworks obtained with L1 (Table 2), the VIS-Slope parameter allows a clear separation - with no need to cut the framework to avoid overlapping - and therefore has a greater capacity than the other parameters to distinguish the three spectral units. The weight assigned is three (Table 3). It could be considered that VIS_Slope L1 has the same reliability as the one obtained with L2 considering its ability to distinguish the spectral units, but since L1 includes all the sampled data also containing the extremes values we give it less reliability.
R750 allows a good distinction between the interior and exterior plains but a modification of the framework is needed to distinguish the LRM from the LBP (Table 2). Therefore, we assign it a lower weight than the VIS_Slope: two (Table 3).
Concerning the UV_Downturn and the VISNIR_Slope, the distinction of the 3 units is only possible after modification of frameworks for all the spectral parameters, showing a weaker capacity for these parameters to spectrally separate LRM, LBP and HRP (Table 2). The weight assigned is one (Table 3).
If the properties of the footprint do not fit into any of the framework for any spectral parameters, then the footprint will not be associated with either the LRM, LBP or HRP. The attributed value is zero (Table 3).
Then for each footprint the total of the marks obtained for each spectral parameter is added up giving a quality parameter out of 16 (Table 3).

Quality parameter	None	L1	L2
VIS-Slope	0	3	4
R750	0	2	4
UV-Downturn	0	1	4
VISNIR-Slope	0	1	4
Total	/16		

Table 3: Quality parameter. Assignment of different significance to the spectral parameters according to their efficiency in discriminating the LRM from the LBP from the HRP. For all footprints spectral parameters are calculated and according to the results a value over 16 is obtained associating the footprint to one spectral unit, another unit or none of them.

Taking into account the spatial coverage and the areas known to be associated with LRM, LBP or HRP a minimum classification criterion has to be validated for the footprint to be finally accepted as belonging to a spectral unit. For LBP and HRP a minimum parameter of 9/16 must be obtained. For LRM 6/16 must be obtained and an additional filter has been applied, the color ratio 415/750. These thresholds provide sufficient footprints for a robust analysis while at the same time filtering accurately to avoid topography-related footprints that can produce classification errors, shadows make spectra appear darker than they really are. A threshold lower than 9/16 or 6/16 increases the possible ambiguity of classification between 2 units for the footprint while a higher threshold removes the number of footprints weakening the robustness of the analysis. The threshold for the LRM is less restrictive since a spectral parameter is added to the four already used. The color ratio 415/750 has to be ≥ 0.6 for LRM in addition to the other filters. This parameter highlights the LRM without allowing the distinction between interior and exterior smooth plains (Figure 3). Even if this parameter cannot distinguish between LRM and bright crater deposits on its own, it can help to distinguish LRM from LBP and HRP.

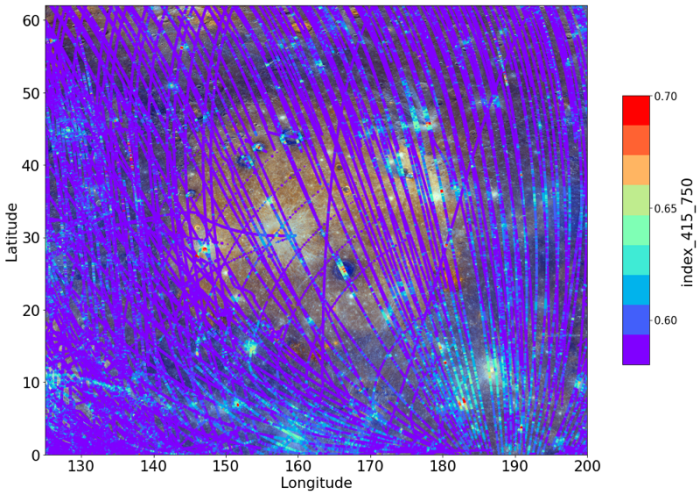

Figure 3: Color Index 415/750 map over the Caloris basin using MASCS footprints. The basemap is a MESSENGER/MDIS enhanced color global mosaic. This parameter highlights LRM and fresh material but it doesn't allow the distinction between interior and exterior plains. This parameter is thus an accurate criterion to help the identification of LRM in comparison with HRP and LBP.

It is now possible to classify every footprint obtained by MASCS/VIRS over the Caloris basin to know if they have spectral properties associated with LRM, LBP or HRP and map these different units. All filtered footprints that belong neither to LRM, LBP nor HRP are considered as unclassified footprints. The methodology and confidence level place any potentially ambiguous footprints under this unclassified category.

3.4 End-member validation

On areas sampled to define a specific spectral unit (Figure 1) we hypothesize that all MASCS footprints belong to the unit being sampled. The spectral mapping was applied

on the sampled areas for LRM, LBP and HRP to verify the hypothesis and the definition of end-members. The spectral mapping shows that not all footprints belong to the sampled unit but that there are some outliers (Figure 4). 2.4% of the footprints sampled on the Caloris exterior plains and used to define the frameworks related to LBP L1 (Table 2) are associated with LRM or HRP. This means that for the statistical analysis and definition of LBP properties 2.4% of the used footprints shall not be considered. Similarly, the percentage of contamination for sampling and spectral definition of HRP L1 within Caloris is 0.2 % and 1.4 % for LRM L1. In order to eliminate this contamination, the statistical analysis was repeated after having removed footprints responsible for the contamination. For the LBP end-member the 2.4% of contaminated footprints were removed and a new statistical analysis similar to the first one was performed on the 97.6% of footprints left including footprints associated with LBP and filtered but unclassified footprints. It was possible to eliminate contamination in the same way for HRP and LRM. The new frameworks obtained (Table 4) are close to those obtained previously but provide a more robust approach in the definition of our 3 end-members. The spectral study of each unit is therefore based on these frameworks (Table 4) and the quality parameter (Table 3).

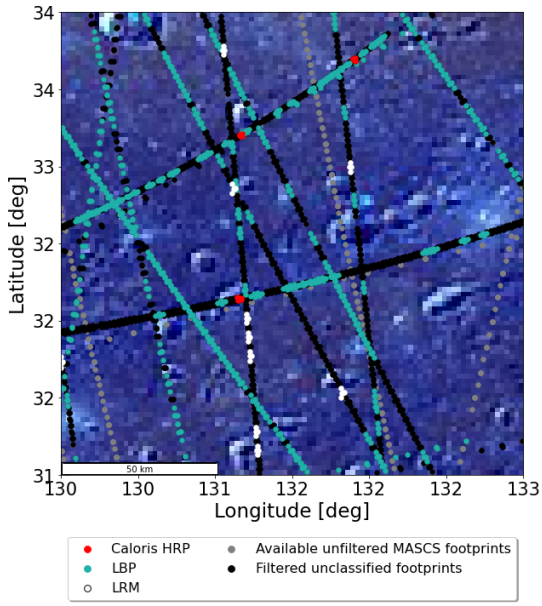

Figure 4: Example of an area within the Caloris exterior plains used for LBP sampling. The basemap is a MESSENGER/MDIS enhanced-color global mosaic. In dark gray are footprints obtained by MASCS with conditions out of the filters (see Section 3.1.2). In green are footprints that have spectral properties associated with the exterior LBP. In red footprints that have spectral properties associated with the interior HRP and in white footprints associated with LRM. In black are footprints that have spectral properties associated neither to interior HRP, exterior LBP nor LRM. This figure highlights footprints that need to be removed for the spectral definition of LBP and confirmation of the end-member.

Spectral units Spectral parameters	Low Reflectance Material	Low-reflectance Blue Plains	High-reflectance Red Plains
Level 1 bis (L1 bis): 100% of the sampled data			
R750	$0.026435 \leq R750 < 0.031196$*	$0.033044 < R750 \leq 0.040640$ *	$0.041681 \leq R750 \leq 0.049263$
VIS_Slope	$0.45548 \leq VIS_{Slope} \leq 0.58906$	$0.62843 \leq VIS_{Slope} \leq 0.81197$	$0.87831 \leq VIS_{Slope} \leq 1.0131$
UV_Downturn	$2.9332 \leq UV_{Downturn} < 2.9828$ *	$3.0844 < UV_{Downturn} < 3.1523$ *	$3.2008 < UV_{Downturn} \leq 3.2651$*
VISNIR_Slope	$0.47230 \leq VISNIR_{Slope} < 0.62486$*	$0.73816 < VISNIR_{Slope} < 0.93423$ *	$0.97032 < VISNIR_{Slope} \leq 1.1714$ *
Level 2 bis (L2 bis): 50% of the sampled data			
R750	$0.028668 \leq R750 \leq 0.030216$	$0.034824 \leq R750 \leq 0.037080$	$0.043680 \leq R750 \leq 0.046584$
VIS_Slope	$0.50615 \leq VIS_{Slope} \leq 0.54764$	$0.70277 \leq VIS_{Slope} \leq 0.75375$	$0.91419 \leq VIS_{Slope} \leq 0.97041$
UV_Downturn	$2.9962 \leq UV_{Downturn} 3.0482$	$3.0724 \leq UV_{Downturn} \leq 3.1240$	$3.1900 \leq UV_{Downturn} \leq 3.2288$
VISNIR_Slope	$0.56161 \leq VISNIR_{Slope} \leq 0.64177$	$0.75144 \leq VISNIR_{Slope} \leq 0.85948$	$1.0192 \leq VISNIR_{Slope} \leq 1.0930$

*Table 4: Frameworks obtained from the statistical analysis of the sampled areas for the study of LRM, LBP and HRP using four spectral parameters after end-members validation. Two confidence levels are studied each using 100% (level 1) and 50% (level 2) of the sampled data. Frames identified by a * were cropped because of an overlap between spectral units.*

It is noticeable that spatially close footprints can have a different classification, especially for unclassified footprints. The methodology and confidence level place any potentially ambiguous footprints under the unclassified category. With a less strict confidence level these same footprints would probably be in the same classification as the closest unit but as they are not part of the quality parameters validating the spectral nature of the footprints they will remain without spectral association. Another explanation could be through a due related to the topography or illumination effects.

4 Results

4.1 Global investigation of the Caloris basin and method validation

The spectral mapping of units was performed on the Caloris basin area to understand the differences and relation between the interior and exterior volcanic smooth plains (Figure 5). MASCS/VIRS footprints (McClintock & Lankton, 2007) are elliptical and extremities are defined by four points with an additional one in the center of the footprint. Each footprint has a spectrum obtained from the integrated signal received

from the surface. This spectrum is analyzed to determine whether the spectral properties correspond to LRM, LBP or HRP. Subsequently, each of the points defining the footprint will be mapped as LRM, LBP or HRP or none of these. Filters applied for temperature, incidence angle and footprint size (see 3.1.2) remove almost 50% of MASCS footprints over the interior and exterior plains (Figure 5) but 101,512 footprints remain usable. Of the usable filtered footprints 26% are associated with LBP, 7% with HRP and 0.6% with LRM. Other footprints belong to the unclassified category.

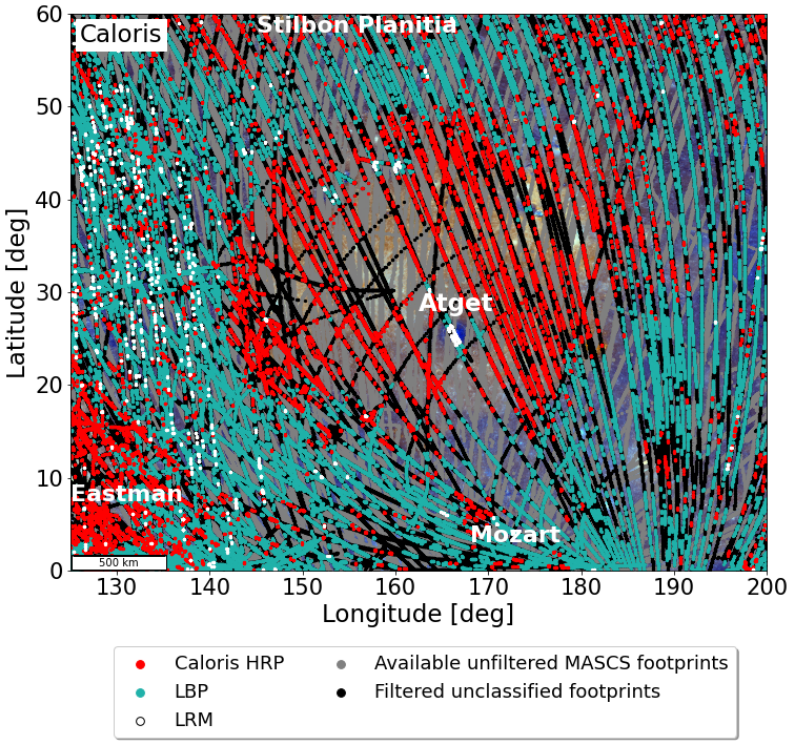

Figure 5: Spectral mapping of the Caloris basin composed of Mercury MESSENGER/MDIS basemap enhanced-color global mosaic on which MASCS/VIRS footprints are plotted according to the spectral classification criteria. Footprints filtered out for temperature, angle of incidence and footprint size are shown in dark gray. Footprints in red have spectral properties associated with HRP, those in green are associated with LBP and footprints in white are associated with LRM. Footprints in black are unclassified.

The interior and exterior plains are well represented and distinguished as HRP and LBP, respectively (Figure 5). HRP footprints are also located north of the basin within Stilbon Planitia, also composed of smooth plains. Other areas mapped as HRP are associated with craters or volcanic high reflectance patches respectively at Mozart and around Eastman crater. Some topography effects around craters can lead to classification errors. The topography has to be considered in order to understand whether the spectral properties of the footprint are related to the ground or biased by a topographic effect. Black footprints are not associated with any spectral unit according to the confidence level, potentially because of topographic effects or because the footprints sample another spectral unit, such as fresh crater materials.

4.2 Interior plains

The MASCS spatial coverage of the interior plains is not complete, especially near the center of the basin (Figure 5) as a lot of footprints were removed. The interior plains are located around a Mercury hot pole at longitude 180° so the instrumental temperature filter removes the majority of footprints (see Section 3.1.2).
The spectral mapping applied on the interior plains shows that all footprints not associated with an impact crater are associated with HRP as expected (Figure 6b). There are several impact craters that occurred after the last volcanic filling of the basin and around which LRM can be observed (Figure 6c). LRM is distributed inside Atget crater as well as on the walls and ejecta of the craters north of the interior plains, Poe (P), Munch (M) and Nahawi (N). LRM is also found on other small craters such as Apollodorus (A) (Figure 6c). These LRM detections are consistent with results obtained by the Mercury Dual Imaging System (MDIS) (Ernst et al., 2010; Ernst et al., 2015; Klima et al., 2018). Around those craters, footprints with spectral properties associated with exterior LBP are also observed (Figure 6a).

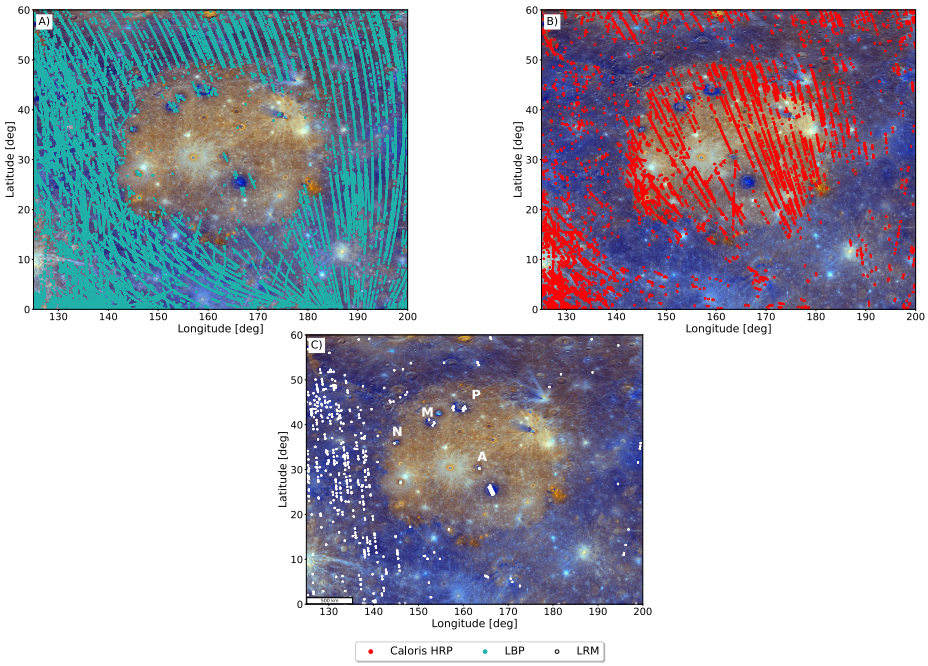

Figure 6: Individual spectral units over the Caloris basin. The basemap is a MESSENGER/MDIS enhanced-color global mosaic. A) Footprints having spectral properties associated with LBP. B) Footprints having spectral properties associated with the HRP. C) Footprints associated with LRM. The letters correspond to the Poe, Munch, Nahawi and Apollodorus craters.

Detailed study of Atget crater reveals LRM in its center (Figure 7a). From the center of the crater to a few hundred kilometers away, footprints show properties of the 3 different spectral units. The LRM deposit is surrounded by exterior plains deposit (LBP) before encountering the spectral properties of the interior plains (HRP) further away from the crater (Figure 7a).

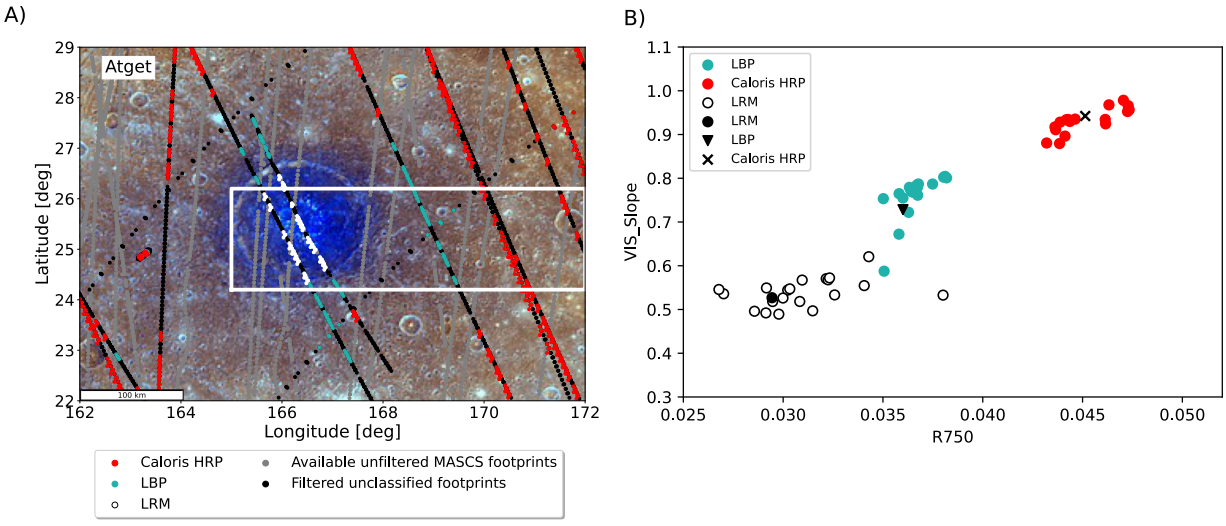

Figure 7: A) Spectral mapping of the Atget crater located on the interior volcanic smooth plains of the Caloris basin. B) The graphic shows the evolution of the spectral properties of the surface between the center of the crater and about 200 km around (white box). The average value for 100% of sampled data L1 bis are represented in black dots for each unit.

Except around the recent craters the interior plain is spectrally homogeneous. The exterior plain is more complex, composed of different geological units and presents spectral heterogeneities.

4.3 Exterior plains

The surroundings of Caloris can be divided into the following geologic units (Trask & Guest ., 1975; Mccauley et al., 1981; Fassett et al., 2009; Denevi et al., 2013; Mancinelli et al., 2016; Guzzetta et al., 2017): smooth plains, the Odin Formation, the Van Eyck Formation (radial geological structures around the basin), the Caloris Montes (topographic rim around the basin), the Nervo Formation (smooth plains located on the Caloris Montes massifs) and the Caloris Rough Ejecta (hummocky and undulating materials surrounding the Caloris basin showing clear boundaries in comparison with the Odin Formation). The most extensive unit is the smooth plains unit while the others are present as small regions mostly associated with the rim (Fassett et al., 2009; Denevi et al., 2013). The Odin formation is a hummocky terrain composed of kilometer-scale knobs and located adjacent to the Caloris rim (Trask & Guest., 1975; Mccauley et al., 1981). The formation covers 2% of the Mercury's surface and it is likely that the knobs are related to impact ejecta, which were then buried by volcanic plains during the emplacement of the exterior plains (Fassett et al., 2009; Head et al., 2009; Denevi et al., 2013). A recent study suggests that these knobs are modified ejecta blocks from Caloris. Mass-wasting, possibly driven by volatile-loss, has resulted in their present shape (Wright et al., 2020). According to MDIS color properties, all the listed geological units that compose the exterior plains of Caloris are

indistinguishable from each other and our MASCS data show the same result (Figure 6a) (Murchie et al., 2008; Murchie et al., 2015; Rothery et al., 2017). Around Caloris we observe an annulus of LBP, with no distinction of the Odin Formation or other geological units (Figure 6a). These spectral observations match with the compositional data that don't show any unit associated with the exterior units (Weider at al., 2015; Nittler et al., 2020).

The western part of the exterior plains is relatively rich in LRM while there is almost no LRM located on the eastern part (Figure 6c). The western LRM is not always associated with craters as in the interior plains but more distributed in the area. By comparing the LRM footprints with the MDIS enhanced color mosaics, we observe that the LRM is located in a slightly "bluer" part than it is in the east of the basin (Figure 8a). Looking at the geology we can see that the western part is mainly composed of smooth plains while the eastern part is more varied showing also the Odin formation and the Van Eyck formation (Figure 8b). No direct correlation between the Odin Formation and LRM is observed. Comparing the distribution of the LRM with the major element composition maps obtained from the MESSENGER/XRS data, there is a similar distribution between the LRM and a region with lower aluminum ratios (Figure 8c) (Weider et al., 2015; Nittler et al., 2020). Indeed, the plains west of Caloris are aluminum-poor compared with the plains east of the basin. The slight difference in the extent of the LRM and the Al-poor zone might be explained by a variation in resolution within the compositional map (Nittler et al., 2020). Furthermore, Nittler et al., 2020 have previously highlighted a link between LRM and Al-poor areas. In addition, there is a weak enrichment of magnesium, also associated with the LRM, in the plains west of Caloris compared to the plains east of the basin (Figure 8d) (Nittler et al., 2020). The elevation does not show any variation east or west of the basin (Figure 8e). The crustal thickness is slightly thicker west of the basin than east of the basin (Figure 8f) (Becker et al., 2016; Beuthe et al., 2020). The non-homogeneous distribution of the LRM between the western and the eastern part of the Caloris exterior plains may be related to the impact formation process (oblique impact) which resulted in heterogeneous deposits around the crater. Moreover, not all of the deep material is necessarily homogeneous across the entire studied area (Ernst et al., 2010). The occurrence of spectral and compositional heterogeneities on the surface in proximity of impact basin such as Caloris can be explained by the presence of both vertical and horizontal heterogeneities in the shallow crust of Mercury (D'Incecco et al., 2015, 2016). Thus, it is also possible that an area of the crust rich in LRM was sampled in the western part of the basin leading to LRM deposits but was not present in the eastern part crust.

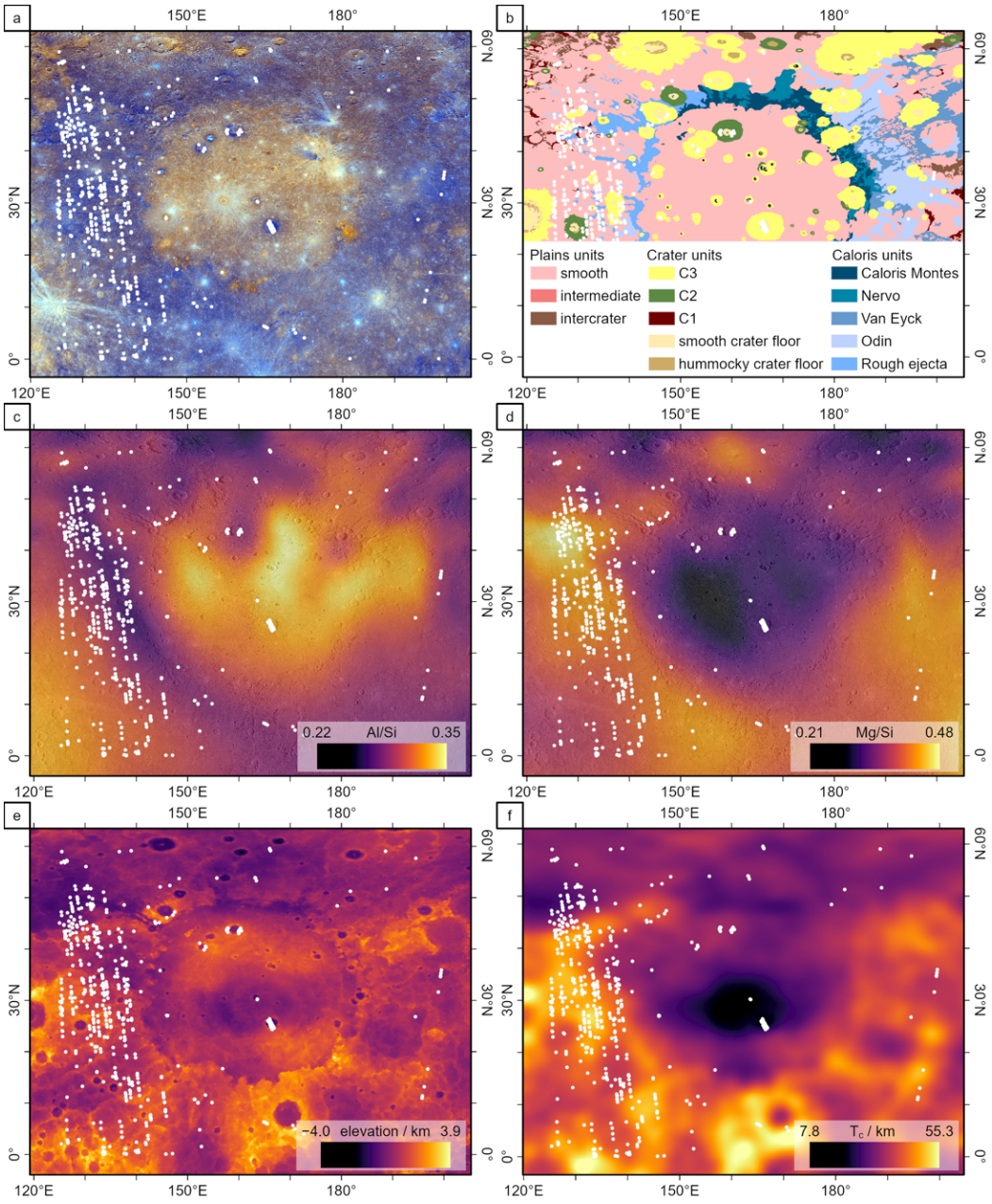

Figure 8: Distribution of LRM in comparison with several parameters. a) MESSENGER MDIS enhanced-color global mosaic obtained by a Principal Component Analysis and published by the Johns Hopkins Applied Physics Laboratory; b) Geological map (Mancinelli et al., 2016; Guzzetta et al., 2017); c) Global major-element maps Al/Si d) Global major-element maps Mg/Si (Nittler et al., 2020); e) Surface elevation map (Becker et al., 2016); f) Crustal thickness (Beuthe et al., 2020).

5 Discussion

5.1 Relative timing for interior and exterior plains from morphology and spectral observations

After the formation of the basin, several steps led to the Caloris basin as we know it today. As the exterior and interior volcanic plains postdate the formation of the Caloris basin although emplaced in a short overlapping period of time, their relative timing is challenging to estimate. Previous results from the analysis of MDIS data brought information that help to clarify the relative age of the interior and exterior plains. Denevi et al, 2013 followed by Rothery et al, 2017 have highlighted different areas where a flow is observed from the exterior plains to the interior plains. However, no signatures with a lower reflectance are observed on the interior plain in these areas showing that the volcanic filling within the basin postdates the flow observed from the exterior LBP to the interior HRP. Observations obtained with the study of Atget crater provide more information on the relative timing of the setting of the interior and exterior plains. In line with the previous flow observations our study supports exterior plains set up before the interior plains. This study highlights a remarkable disposition of spectral units around the Atget crater where LRM is concentrated inside the crater and is surrounded by footprints associated with exterior LBP before being surrounded by HRP characteristic of the interior plains. Atget can be used to reconstruct the subjacent stratigraphy. Indeed, the area is not disturbed by any tectonic event and it is therefore possible to apply the geological principles of superposition. According to crater ejecta deposition, this arrangement indicates a deep LRM layer, succeeded by a layer of LBP and finally HRP, the deepest layer always being located at the center of the crater (Stöffler et al., 1975; Osinski et al., 2022). These observations provide information on the relative timing of the setting of the exterior and interior plains.
Following the impact, a layer of impact melt and LRM was deposited in the crater (Ernst et al., 2010,2015). The exterior plains were then formed by a widespread effusive volcanism, forming a LBP unit inside and around the basin covering the impact melt deposits. Afterwards, the interior plains were emplaced by effusive volcanism, within the basin only, forming the HRP unit. The thickness of the actual interior volcanic HRP layer was estimated by Ernst et al., 2015 at around 2.5 - 4 km (later confirmed by Hirata et al., 2022). These studies are based on a homogeneous HRP volcanic layer superimposed on LRM deposits excavated by the basin formation. However, we have shown that there is not a single volcanic layer that participated in the filling of the basin but two volcanic layers. One layer of volcanic LBP stratigraphically above the LRM deposit inside the basin and a layer of volcanic HRP visible on the surface. The thickness of the HRP layer must therefore be revised downwards.

The thermal pulse from an impact as large as the one that created the Caloris basin can alter the underlying mantle dynamics and produce subsequent volcanism (Roberts

& Barnouin., 2012). Post-impact melting could occur on a large time scale after the impact up to hundreds of millions of years (Elkins-Tanton et al., 2004; Padovan et al., 2017). Volcanism already active or the thermal anomaly created post-impact (Roberts & Barnouin, 2012) would have led to extended volcanism in and around the Caloris basin (Wang et al., 2021). These deposits would still be visible and would represent the exterior LBP. Subsequently, a second stage of volcanism would have filled the basin burying the first volcanic LBP deposits and creating the interior HRP. The time between the two volcanic events would be the reason for the spectral and composition differences between the interior and exterior plains and it is clear that an evolution of magmatism processes occurred during this time. Understanding this evolution will clarify our understanding of hermean magmatism in link with impact formation, including the nature and depth of volcanic sources and the degree of partial melting (Weider et al., 2013; Wang et al., 2022).

This result about relative timing with the study of Atget is based on the observation that around the Atget crater, LRM is concentrated in the center followed by a deposit of LBP and then a deposit of HRP. Another hypothesis to interpret this disposition of spectral units could be that the LBP observation is in reality a mixing between LRM and HRP that mimics the LBP spectral properties. However, this hypothesis implies a perfect mixing with the exact amount of HRP and LBP to validate the confidence level and mimic the LBP properties. Moreover, the mixing would have been homogeneous around Atget as there is LBP at the north, south and east of the crater. Finally, Figure 7b shows a clear separation between the three spectral units according to the R750 and the VIS_Slope which goes against the hypothesis of a mixture. Other impact craters located at the north of the interior plains suggest the same stratigraphy obtained with Atget with deposits associated with LBP followed by HRP going outward from the crater (Ernst et al., 2015).

5.2 Compositional data and origin of spectral differences between interior and exterior plains

- 5.2.1 Partial melting degree

The interior volcanic smooth plains of Caloris are poor in Mg and rich in Al. In comparison with the exterior plains that are globally poorer in Al and richer in Mg (Weider et al., 2015; Nittler et al., 2020). Terrestrial rocks such as boninites, basaltic komatiites or komatiites represent good analogs covering the Mg and Al variations of the interior and exterior plains (Stockstill-Cahill et al., 2012; Charlier et al., 2013; Maturilli et al., 2014; Vander Kaaden & McCubbin, 2016; Vander Kaaden et al., 2017). The thickness of the crust beneath the Caloris Basin is the thinnest on Mercury (Beuthe et al., 2020) while the crust beneath the exterior volcanic smooth plains circum-Caloris have a greater thickness (Figure 8f). A correlation exists between

crustal thickness and the mantle melt production (Beuthe et al., 2020). Low-degree mantle melting produces a thin crust in comparison with a high-degree of melting that produces a thicker Mg-rich crust. The thickness of the crust suggests a higher partial melting degree for the emplacement of the exterior plains crust in comparison with the interior plains crust.

During partial melting of a peridotite mantle, the concentration of Mg in the produced lava is lower for a low partial melting degree than for a high partial melting degree that increases the melt fraction. The interior plains thus appear to be derived from magma obtained at a lower partial melting degree than the exterior plains. Namur et al. (2016) have shown that the melt productivity decreases with time on Mercury in line with the secular cooling of the planet. The composition of the interior and exterior plains associated to the thickness of the crust consequently reflects a decrease in the melting degree over time between the formation of the exterior plains followed by the formation of the interior plains in line with our analysis. Furthermore, the elemental composition of the interior plains is consistent with over 50% plagioclase (Vander Kaaden et al., 2017; Namur & Charlier, 2017) and does not contain olivine in comparison with the exterior plains. Namur & Charlier. (2017) have shown that there is a temporal evolution between older, mafic mineral-dominated lavas and younger, plagioclase-rich lavas that is also consistent with our spectral observations.

Over time the planet cooled leading to lavas formed with a lower liquidus temperature. Stockstill-cahill et al. (2012) showed that the liquidus temperature of terrestrial analogues of Mercury's crust decrease with decreasing Mg content of the rock. For Caloris this confirms a decrease in liquidus temperature at the origin of the interior plains compared to the exterior plains over time. Decreasing the temperature through time implies that the magma formed under a lower melt fraction and/or at a lower depth.

We focus this study on Caloris and its associated volcanic plains but for any comparison with other basins and their associated volcanic plains it is important to take into account that although the degree of partial melting decreases over time on Mercury, mantle disrupting events such as major impacts can reverse this trend locally (Wang et al., 2022).

- 5.2.2 Partial melting depth

Besides high degree of partial melting, high pressure melting can also generate lava enriched in Mg. At high pressure around 5 Gpa and more (high depth) Mg-rich silicates preferentially melt and produce lava rich in Mg and poor in Al (Arndt & Lesher, 2004; Stockstill-Cahill et al., 2012). With increasing pressure (and therefore depth) orthopyroxene becomes more stable compared to olivine and garnet becomes more stable compared to other mantle magnesian minerals. The compositional differences between interior and exterior plains could then also be explained by two different melting depths. According to the composition, the melting depth at the origin of the exterior plains would be greater than for the interior plains formation. The pressure

needed for the exterior plains could be around 5 GPa and more that is reached on Mercury at the core-mantle boundary estimated around 5.5 Gpa (420+-30km) (Hauck et al., 2013). The partial melts of the hermean mantle that compose the secondary crust could originate from as far away as the core-mantle boundary (Vander Kaaden & McCubbin, 2015). The depth of melting required for lava formation on Mercury has decreased between the formation of ancient and more recent lavas (Namur et al., 2016) and the study of the Caloris Basin shows that the depth of the volcanic source that fills the basin becomes shallower with time (Padovan et al., 2017) and so between the formation of the exterior and the interior plains. In addition to the variation of the melting rates, the variation of melting depth could also explain the compositional variations between older exterior plains and more recent interior plains.

The connection between internal processes, compositional and spectral differences on the surface of Mercury has not yet been fully clarified but one hypothesis is a rapid cooling of the mantle where the temperature, degree of partial melting and pressure in the melt source regions change rapidly over time. The cooling over time decreases the internal temperature and partial melting degree in the mantle leading to magma with different composition. On Mercury, melting depth decreases with time and major impact events also change the melt source leading to variations in surface lava (Padovan et al., 2017). Our study cannot distinguish whether the origin of the spectral and compositional differences at the surface are due to a decrease in partial melting degree, partial melting depth or most likely both. However, we have shown that both decreasing partial melting degree and decreasing partial melting depth have actively modified magma production over a short period of time on Mercury and can explain the surface properties validating the relative timing of Caloris' volcanic smooth plains.

6 Conclusion

MESSENGER/MASCS data contains information about relationships between impact cratering and effusive volcanism on Mercury as well as evolution of the planet's magmatism over time. A better understanding of volcanism provides a better constraint on the internal evolution of the planet and the formation of the crust over time. Advances in the understanding of the Caloris basin and its interior and exterior associated volcanic smooth plains leads us to conclusions on the timeline of these events and the origin of spectral and compositional differences on the surface.

1. A detailed spectral analysis of the Atget crater has revealed that the exterior plains of the Caloris basin were emplaced both outside and inside the basin before the interior plains were emplaced inside the basin only.

2. On Mercury, the partial melting degree and the melting depth decrease over time. We propose that the interior plains were formed by a lower degree of partial melting and/or melting depth than the exterior plains to explain the origin of their spectral and compositional differences.

3. The exterior volcanic smooth plains of Caloris are spectrally heterogeneous west and east with LRM concentrated on the western part. This area is correlated with an Al poor composition. This suggests a heterogeneous impact ejecta deposit or a laterally discontinuous LRM layer below Caloris.

To constrain the diversity of lavas that erupted on Mercury, Mg rich terrestrial rocks such as boninites, basaltic komatiites or komatiites represent good analogs covering the Mg and Al variations of the interior and exterior plains. (Stockstill-Cahill et al., 2012; Charlier et al., 2013; Maturilli et al., 2014; Vander Kaaden & McCubbin, 2016; Vander Kaaden et al., 2017 ; Mari et al., 2022). A study of the spectral properties of these analogs under Mercury's temperature and space weathering conditions could help to explain more in detail the spectral differences discussed in this work.

The relationship between impact cratering and volcanism, magmagenesis and more globally the history of crustal formation are major ongoing science questions that motivated the ESA/JAXA/BepiColombo mission (Rothery et al., 2020).

Acknowledgments

The authors acknowledge the Centre National des Etudes Spatiales (CNES) for continuous and long-term support. We acknowledge the Domaine d'Intérêt Majeur en Astrophysique et Conditions d'Apparition de la Vie+ île de France for their support. E. Caminiti acknowledges the support of the European Space Astronomy Centre (ESAC) faculty council for funding visits to ESAC as part of this work. J. Wright acknowledges support from the European Space Agency (ESA) as an ESA Research Fellow. The authors acknowledge Piero D'Incecco, Deanne Rogers, the anonymous referee and associate editor for their detailed and helpful comments at the review stage.

Data Availability Statement

All data used in this work are accessible in Caminiti,E. (2023). The document contains reflectance spectra from PDS Geosciences Node of Washington University, St.Louis, MO, USA (McClintock and Lankton, 2007) corrected by the methodology developed by Besse et al., 2015 as well as the latitude and longitude of every footprint used in the present work. All spectral parameters can be calculated directly using this document.

References

Arndt, N., & Lesher, C. M. (2004). Komatiite. hal-00101712

Bauch, K. E., Hiesinger, H., Greenhagen, B. T., & Helbert, J. (2021). Estimation of surface temperatures on Mercury in preparation of the MERTIS experiment onboard BepiColombo. *Icarus*, *354*, 114083. https://doi.org/10.1016/j.icarus.2020.114083

Barraud, O., Doressoundiram, A., Besse, S., & Sunshine, J. M. (2020). Near-Ultraviolet to Near-Infrared Spectral Properties of Hollows on Mercury: Implications for Origin and Formation Process. *Journal of Geophysical Research: Planets*, *125*(12), e2020JE006497. https://doi.org/10.1029/2020JE006497

Barraud, O., Besse, S., Doressoundiram, A., Cornet, T., & Muñoz, C. (2021). Spectral investigation of Mercury's pits' surroundings: Constraints on the planet's explosive activity. *Icarus*, *370*, 114652. https://doi.org/10.1016/j.icarus.2021.114652

Becker, K. J., Robinson, M. S., Becker, T. L., Weller, L. A., Edmundson, K. L., Neumann, G. A., ... & Solomon, S. C. (2016, March). First global digital elevation model of Mercury. In *47th Annual Lunar and Planetary Science Conference* (No. 1903, p. 2959).

Besse, S., Doressoundiram, A., & Benkhoff, J. (2015). Spectroscopic properties of explosive volcanism within the Caloris basin with MESSENGER observations. *Journal of Geophysical Research: Planets*, *120*(12), 2102-2117. https://doi.org/10.1002/2015JE004819

Besse, S., Doressoundiram, A., Barraud, O., Griton, L., Cornet, T., Muñoz, C., ... & Helbert, J. (2020). Spectral properties and physical extent of pyroclastic deposits on Mercury: Variability within selected deposits and implications for explosive volcanism. *Journal of Geophysical Research: Planets*, *125*(5), e2018JE005879. https://doi.org/10.1029/2018JE005879

Besse, S., Cornet, T., Munoz, C., Barraud, O., Noam, I., Doressoundiram, A., & Caminiti, E. (2022). Updating the Mercury Mean Spectra using 4.7 millions MASCS Spectra. Mercury 2022 conference, *Orléans, France, 7-10 June 2022*, 61.

Beuthe, M., Charlier, B., Namur, O., Rivoldini, A., & Van Hoolst, T. (2020). Mercury's crustal thickness correlates with lateral variations in mantle melt production. *Geophysical Research Letters*, *47*(9), e2020GL087261. https://doi.org/10.1029/2020GL087261

Blewett, D. T., Vaughan, W. M., Xiao, Z., Chabot, N. L., Denevi, B. W., Ernst, C. M., ... & Solomon, S. C. (2013). Mercury's hollows: Constraints on formation and composition from analysis of geological setting and spectral reflectance. *Journal of Geophysical Research: Planets*, *118*(5), 1013-1032. https://doi.org/10.1029/2012JE004174

Bott, N., Doressoundiram, A., Zambon, F., Carli, C., Guzzetta, L., Perna, D., & Capaccioni, F. A. B. R. I. Z. I. O. (2019). Global spectral properties and lithology of Mercury: The example of the Shakespeare (H-03) quadrangle. *Journal of Geophysical Research: Planets*, *124*(9), 2326-2346. https://doi.org/10.1029/2019JE005932

Byrne, P. K., Ostrach, L. R., Fassett, C. I., Chapman, C. R., Denevi, B. W., Evans, A. J., ... & Solomon, S. C. (2016). Widespread effusive volcanism on Mercury likely ended by about 3.5 Ga. *Geophysical Research Letters*, *43*(14), 7408-7416. https://doi.org/10.1002/2016GL069412

Byrne, P. K. (2020). A comparison of inner Solar System volcanism. *Nature Astronomy*, *4*(4), 321-327. https://doi.org/10.1038/s41550-019-0944-3

Caminiti, Emma. (2023). The Mess data used in “A spectral study of the Caloris basin on Mercury and the origin of associated volcanic smooth plains” [Data set]. Zenodo. http://doi.org/10.5281/zenodo.7682217

Charlier, B., Grove, T. L., & Zuber, M. T. (2013). Phase equilibria of ultramafic compositions on Mercury and the origin of the compositional dichotomy. *Earth and Planetary Science Letters*, *363*, 50-60. https://doi.org/10.1016/j.epsl.2012.12.021

Cornet, T., Besse, S., Munoz, C., Barraud, O., & Doressoundiram, A. (2022). Exploring the MASCS data set through the MeSS database. *Mercury 2022*, 71-71.

Denevi, B. W., Robinson, M. S., Solomon, S. C., Murchie, S. L., Blewett, D. T., Domingue, D. L., ... & Chabot, N. L. (2009). The evolution of Mercury’s crust: A global perspective from MESSENGER. *Science*, *324*(5927), 613-618. https://doi.org/10.1126/science.1172226

Denevi, B. W., Ernst, C. M., Meyer, H. M., Robinson, M. S., Murchie, S. L., Whitten, J. L., ... & Peplowski, P. N. (2013). The distribution and origin of smooth plains on Mercury. *Journal of Geophysical Research: Planets*, *118*(5), 891-907. https://doi.org/10.1002/jgre.20075

D’Incecco, P., Helbert, J., D’Amore, M., Maturilli, A., Head, J. W., Klima, R. L., ... & Ferrari, S. (2015). Shallow crustal composition of Mercury as revealed by spectral properties and geological units of two impact craters. *Planetary and Space Science*, *119*, 250-263. https://doi.org/10.1016/j.pss.2015.10.007

D’Incecco, P., Helbert, J., D’Amore, M., Ferrari, S., Head, J. W., Maturilli, A., and Hiesinger, H., 2016. A geologically supervised spectral analysis of 121 globally distributed impact craters as a tool for identifying vertical and horizontal heterogeneities in the composition of the shallow crust of Mercury. Planetary and Space Science, Volume 132, p. 32-56, https://doi.org/10.1016/j.pss.2016.08.004

Elkins-Tanton, L. T., Hager, B. H., & Grove, T. L. (2004). Magmatic effects of the lunar late heavy bombardment. *Earth and Planetary Science Letters*, *222*(1), 17-27. https://doi.org/10.1016/j.epsl.2004.02.017

Ernst, C. M., Murchie, S. L., Barnouin, O. S., Robinson, M. S., Denevi, B. W., Blewett, D. T., ... & Roberts, J. H. (2010). Exposure of spectrally distinct material by impact craters on Mercury: Implications for global stratigraphy. *Icarus*, *209*(1), 210-223. https://doi.org/10.1016/j.icarus.2010.05.022

Ernst, C. M., Denevi, B. W., Barnouin, O. S., Klimczak, C., Chabot, N. L., Head, J. W., ... & Watters, T. R. (2015). Stratigraphy of the Caloris basin, Mercury: Implications for volcanic history and basin impact melt. *Icarus*, *250*, 413-429. https://doi.org/10.1016/j.icarus.2014.11.003

Fassett, C. I., Head, J. W., Blewett, D. T., Chapman, C. R., Dickson, J. L., Murchie, S. L., ... & Watters, T. R. (2009). Caloris impact basin: Exterior geomorphology, stratigraphy, morphometry, radial sculpture, and smooth plains deposits. *Earth and Planetary Science Letters*, *285*(3-4), 297-308. https://doi.org/10.1016/j.epsl.2009.05.022

Fassett, C. I., Head, J. W., Baker, D. M., Zuber, M. T., Smith, D. E., Neumann, G. A., ... & Preusker, F. (2012). Large impact basins on Mercury: Global distribution, characteristics, and modification history from MESSENGER orbital data. *Journal of Geophysical Research: Planets*, *117*(E12). https://doi.org/10.1029/2012JE004154

Goudge, T. A., Head, J. W., Kerber, L., Blewett, D. T., Denevi, B. W., Domingue, D. L., ... & Solomon, S. C. (2014). Global inventory and characterization of pyroclastic deposits on Mercury: New insights into pyroclastic activity from MESSENGER orbital data. *Journal of Geophysical Research: Planets*, *119*(3), 635-658. https://doi.org/10.1002/2013JE004480

Guzzetta, L., Galluzzi, V., Ferranti, L., & Palumbo, P. (2017). Geology of the Shakespeare quadrangle (H03), Mercury. *Journal of Maps*, *13*(2), 227-238. https://doi.org/10.1080/17445647.2017.1290556

Hauck, S. A., Margot, J. L., Solomon, S. C., Phillips, R. J., Johnson, C. L., Lemoine, F. G., ... & Zuber, M. T. (2013). The curious case of Mercury's internal structure. *Journal of Geophysical Research: Planets*, *118*(6), 1204-1220. https://doi.org/10.1002/jgre.20091

Head, J. W., Murchie, S. L., Prockter, L. M., Robinson, M. S., Solomon, S. C., Strom, R. G., ... & Gillis-Davis, J. J. (2008). Volcanism on Mercury: Evidence from the first MESSENGER flyby. *Science*, *321*(5885), 69-72. https://doi.org/10.1126/science.1159256

Head, J. W., Murchie, S. L., Prockter, L. M., Solomon, S. C., Chapman, C. R., Strom, R. G., ... & Kerber, L. (2009). Volcanism on Mercury: Evidence from the first MESSENGER flyby for extrusive and explosive activity and the volcanic origin of plains. *Earth and Planetary Science Letters*, *285*(3-4), 227-242. https://doi.org/10.1016/j.epsl.2009.03.007

Head, J. W., Chapman, C. R., Strom, R. G., Fassett, C. I., Denevi, B. W., Blewett, D. T., ... & Nittler, L. R. (2011). Flood volcanism in the northern high latitudes of Mercury revealed by MESSENGER. *Science*, *333*(6051), 1853-1856. https://doi.org/10.1126/science.1211997

Hirata, K., Morota, T., Sugita, S., Ernst, C. M., & Usui, T. (2022). Magma eruption ages and fluxes in the Rembrandt and Caloris interior plains on Mercury: Implications for the north-south smooth plains asymmetry. *Icarus*, *382*, 115034. https://doi.org/10.1016/j.icarus.2022.115034

Izenberg, N. R., Klima, R. L., Murchie, S. L., Blewett, D. T., Holsclaw, G. M., McClintock, W. E., ... & Dyar, M. D. (2014). The low-iron, reduced surface of Mercury as seen in spectral reflectance by MESSENGER. *Icarus*, *228*, 364-374. https://doi.org/10.1016/j.icarus.2013.10.023

Klima, R. L., Denevi, B. W., Ernst, C. M., Murchie, S. L., & Peplowski, P. N. (2018). Global distribution and spectral properties of low-reflectance material on Mercury. *Geophysical Research Letters*, *45*(7), 2945-2953. https://doi.org/10.1002/2018GL077544

Kiefer, W. S., & Murray, B. C. (1987). The formation of Mercury's smooth plains. *Icarus*, *72*(3), 477-491. https://doi.org/10.1016/0019-1035(87)90046-7

Kinczyk, M. J., Prockter, L. M., Byrne, P. K., Susorney, H. C., & Chapman, C. R. (2020). A morphological evaluation of crater degradation on Mercury: Revisiting crater classification with MESSENGER data. *Icarus*, *341*, 113637. https://doi.org/10.1016/j.icarus.2020.113637

Mancinelli, P., Minelli, F., Pauselli, C., & Federico, C. (2016). Geology of the Raditladi quadrangle, Mercury (H04). *Journal of Maps*, *12*(sup1), 190-202. https://doi.org/10.1080/17445647.2016.1191384

Marchi, S., Massironi, M., Cremonese, G., Martellato, E., Giacomini, L., & Prockter, L. (2011). The effects of the target material properties and layering on the crater chronology: The case of Raditladi and Rachmaninoff basins on Mercury. *Planetary and Space Science*, *59*(15), 1968-1980. https://doi.org/10.1016/j.pss.2011.06.007

Marchi, S., Chapman, C. R., Fassett, C. I., Head, J. W., Bottke, W. F., & Strom, R. G. (2013). Global resurfacing of Mercury 4.0–4.1 billion years ago by heavy bombardment and volcanism. *Nature*, *499*(7456), 59-61. https://doi.org/10.1038/nature12280

Mari N., Eggers G. L., Filiberto J., Pratesi G., Carli C., Alvaro M., and D'Incecco P., 2022. Boninites from Cyprus Island as Mercury lava analogues.23rd International Mineralogical Association General Meeting, Abstract# 1113, Lyon (France).

Maturilli, A., Helbert, J., John, J. M. S., Head III, J. W., Vaughan, W. M., D'Amore, M., ... & Ferrari, S. (2014). Komatiites as Mercury surface analogues: spectral measurements at PEL. *Earth and Planetary Science Letters*, *398*, 58-65. https://doi.org/10.1016/j.epsl.2014.04.035

Mccauley, J. F., Guest, J. E., Schaber, G. G., Trask, N. J., & Greeley, R. (1981). Stratigraphy of the Caloris basin, Mercury. *Icarus*, *47*(2), 184-202. https://doi.org/10.1016/0019-1035(81)90166-4

McClintock, W. E., & Lankton, M. R. (2007). The Mercury atmospheric and surface composition spectrometer for the MESSENGER mission. *Space Science Reviews*, *131*(1), 481-521. https://doi.org/10.1007/s11214-007-9264-5

McNutt Jr, R. L., Solomon, S. C., Gold, R. E., Leary, J. C., & MESSENGER Team. (2006). The MESSENGER mission to Mercury: Development history and early mission status. *Advances in Space Research*, *38*(4), 564-571. https://doi.org/10.1016/j.asr.2005.05.044

Murray, B. C., Strom, R. G., Trask, N. J., & Gault, D. E. (1975). Surface history of Mercury: Implications for terrestrial planets. *Journal of Geophysical Research*, *80*(17), 2508-2514. https://doi.org/10.1029/JB080i017p02508

Murchie, S. L., Watters, T. R., Robinson, M. S., Head, J. W., Strom, R. G., Chapman, C. R., ... & Blewett, D. T. (2008). Geology of the Caloris basin, Mercury: A view from MESSENGER. *science*, *321*(5885), 73-76. https://doi.org/10.1126/science.1159261

Murchie, S. L., Klima, R. L., Denevi, B. W., Ernst, C. M., Keller, M. R., Domingue, D. L., ... & Solomon, S. C. (2015). Orbital multispectral mapping of Mercury with the MESSENGER Mercury Dual Imaging System: Evidence for the origins of plains units and low-reflectance material. *Icarus*, *254*, 287-305. https://doi.org/10.1016/j.icarus.2015.03.027

Namur, O., Collinet, M., Charlier, B., Grove, T. L., Holtz, F., & McCammon, C. (2016). Melting processes and mantle sources of lavas on Mercury. *Earth and Planetary Science Letters*, *439*, 117-128. https://doi.org/10.1016/j.epsl.2016.01.030

Namur, O., & Charlier, B. (2017). Silicate mineralogy at the surface of Mercury. *Nature Geoscience*, *10*(1), 9-13. https://doi.org/10.1038/ngeo2860

Nittler, L. R., Frank, E. A., Weider, S. Z., Crapster-Pregont, E., Vorburger, A., Starr, R. D., & Solomon, S. C. (2020). Global major-element maps of Mercury from four years of MESSENGER X-Ray Spectrometer observations. *Icarus*, *345*, 113716. https://doi.org/10.1016/j.icarus.2020.113716

Oberbeck, V. R., Quaide, W. L., Arvidson, R. E., & Aggarwal, H. R. (1977). Comparative studies of lunar, martian, and mercurian craters and plains. *Journal of Geophysical Research*, *82*(11), 1681-1698. https://doi.org/10.1029/JB082i011p01681

Osinski, G. R., Grieve, R. A., Ferrière, L., Losiak, A., Pickersgill, A., Cavosie, A. J., ... & Simpson, S. L. (2022). Impact Earth: A review of the terrestrial impact record. *Earth-Science Reviews*, 104112. https://doi.org/10.1016/j.earscirev.2022.104112

Padovan, S., Tosi, N., Plesa, A. C., & Ruedas, T. (2017). Impact-induced changes in source depth and volume of magmatism on Mercury and their observational signatures. *Nature communications*, *8*(1), 1-10. https://doi.org/10.1038/s41467-017-01692-0

Peplowski, P. N., Lawrence, D. J., Feldman, W. C., Goldsten, J. O., Bazell, D., Evans, L. G., ... & Weider, S. Z. (2015). Geochemical terranes of Mercury's northern hemisphere as revealed by MESSENGER neutron measurements. *Icarus*, *253*, 346-363. https://doi.org/10.1016/j.icarus.2015.02.002

Peplowski, P. N., Klima, R. L., Lawrence, D. J., Ernst, C. M., Denevi, B. W., Frank, E. A., ... & Solomon, S. C. (2016). Remote sensing evidence for an ancient carbon-bearing crust on Mercury. *Nature Geoscience*, *9*(4), 273-276. https://doi.org/10.1038/ngeo2669

Roberts, J. H., & Barnouin, O. S. (2012). The effect of the Caloris impact on the mantle dynamics and volcanism of Mercury. *Journal of Geophysical Research: Planets*, *117*(E2). https://doi.org/10.1029/2011JE003876

Robinson, M. S., Murchie, S. L., Blewett, D. T., Domingue, D. L., Hawkins III, S. E., Head, J. W., ... & Watters, T. R. (2008). Reflectance and color variations on Mercury: Regolith processes and compositional heterogeneity. *science*, *321*(5885), 66-69. https://doi.org/10.1126/science.1160080

Rothery, D. A., Mancinelli, P., Guzzetta, L., & Wright, J. (2017). Mercury's Caloris basin: Continuity between the interior and exterior plains. *Journal of Geophysical Research: Planets*, *122*(3), 560-576. https://doi.org/10.1002/2017JE005282

Rothery, D. A., Massironi, M., Alemanno, G., Barraud, O., Besse, S., Bott, N., ... & Zambon, F. (2020). Rationale for BepiColombo studies of Mercury's surface and composition. *Space science reviews*, *216*, 1-46. https://doi.org/10.1007/s11214-020-00694-7

Solomon, S. C., McNutt, R. L., Gold, R. E., & Domingue, D. L. (2007). MESSENGER mission overview. Space Science Reviews, 131(1–4), 3–39. https://doi.org/10.1007/s11214-007-9247-6

Spudis, P. D., & Guest, J. E. (1988). Stratigraphy and geologic history of Mercury. *Mercury*, 118-164.

Stockstill-Cahill, K. R., McCoy, T. J., Nittler, L. R., Weider, S. Z., & Hauck, S. A. (2012). Magnesium-rich crustal compositions on Mercury: Implications for magmatism from petrologic modeling. *Journal of Geophysical Research: Planets*, *117*(E12). https://doi.org/10.1029/2012JE004140

Stöffler, D., Gault, D. E., Wedekind, J., & Polkowski, G. (1975). Experimental hypervelocity impact into quartz sand: Distribution and shock metamorphism of ejecta. *Journal of Geophysical Research*, *80*(29), 4062-4077. https://doi.org/10.1029/JB080i029p04062

Strom, R. G., Trask, N. J., & Guest, J. E. (1975). Tectonism and volcanism on Mercury. *Journal of Geophysical Research*, *80*(17), 2478-2507. https://doi.org/10.1029/JB080i017p02478

Strom, R. G., Chapman, C. R., Merline, W. J., Solomon, S. C., & Head III, J. W. (2008). Mercury cratering record viewed from MESSENGER's first flyby. *Science*, *321*(5885), 79-81. https://doi.org/10.1126/science.1159317

Strom, R. G., Banks, M. E., Chapman, C. R., Fassett, C. I., Forde, J. A., Head III, J. W., ... & Solomon, S. C. (2011). Mercury crater statistics from MESSENGER flybys: Implications for stratigraphy and resurfacing history. *Planetary and Space Science*, *59*(15), 1960-1967. https://doi.org/10.1016/j.pss.2011.03.018

Trask, N. J., & Guest, J. E. (1975). Preliminary geologic terrain map of Mercury. *Journal of Geophysical Research*, *80*(17), 2461-2477. https://doi.org/10.1029/JB080i017p02461

Vander Kaaden, K. E., & McCubbin, F. M. (2015). Exotic crust formation on Mercury: Consequences of a shallow, FeO-poor mantle. *Journal of Geophysical Research: Planets*, *120*(2), 195-209. https://doi.org/10.1002/2014JE004733

Vander Kaaden, K. E., & McCubbin, F. M. (2016). The origin of boninites on Mercury: An experimental study of the northern volcanic plains lavas. *Geochimica et Cosmochimica Acta*, *173*, 246-263. https://doi.org/10.1016/j.gca.2015.10.016

Vander Kaaden, K. E., McCubbin, F. M., Nittler, L. R., Peplowski, P. N., Weider, S. Z., Frank, E. A., & McCoy, T. J. (2017). Geochemistry, mineralogy, and petrology of boninitic and komatiitic rocks on the mercurian surface: Insights into the mercurian mantle. *Icarus*, *285*, 155-168. https://doi.org/10.1016/j.icarus.2016.11.041

Wang, Y., Xiao, Z., Chang, Y., Xu, R., & Cui, J. (2021). Short-Term and Global-Wide Effusive Volcanism on Mercury Around 3.7 Ga. *Geophysical Research Letters*, *48*(20), e2021GL094503. https://doi.org/10.1029/2021GL094503

Wang, Y., Xiao, Z., & Xu, R. (2022). Multiple Mantle Sources of High-Magnesium Terranes on Mercury. *Journal of Geophysical Research: Planets*, *127*(5), e2022JE007218. https://doi.org/10.1029/2022JE007218

Weider, S. Z., Nittler, L. R., Denevi, B. W., Starr, R. D., & Solomon, S. C. (2013, December). Mapping the Composition of the Caloris Basin with MESSENGER X-Ray Spectrometer Data. In *AGU Fall Meeting Abstracts* (Vol. 2013, pp. P11A-05).

Weider, S. Z., Nittler, L. R., Starr, R. D., Crapster-Pregont, E. J., Peplowski, P. N., Denevi, B. W., ... & Solomon, S. C. (2015). Evidence for geochemical terranes on Mercury: Global mapping of major elements with MESSENGER's X-Ray Spectrometer. *Earth and Planetary Science Letters*, *416*, 109-120. https://doi.org/10.1016/j.epsl.2015.01.023

Wilhelms, D. E. (1976). Mercurian volcanism questioned. *Icarus*, *28*(4), 551-558. https://doi.org/10.1016/0019-1035(76)90128-7

Wright, J., Conway, S. J., Morino, C., Rothery, D. A., Balme, M. R., & Fassett, C. I. (2020). Modification of Caloris ejecta blocks by long-lived mass-wasting: A volatile-driven process?. *Earth and Planetary Science Letters*, *549*, 116519. https://doi.org/10.1016/j.epsl.2020.116519

Wright, J., Byrne, P. K., & Rothery, D. A. (2021). Planet Mercury: Volcanism in a theatre of global contraction, with examples from the Hokusai quadrangle. *Journal of Volcanology and Geothermal Research*, *417*, 107300. https://doi.org/10.1016/j.jvolgeores.2021.107300

Zambon, F., Carli, C., Wright, J., Rothery, D. A., Altieri, F., Massironi, M., ... & Cremonese, G. (2022). Spectral units analysis of quadrangle H05-Hokusai on Mercury. *Journal of Geophysical Research: Planets*, Early-access. https://doi.org/10.1029/2021je006918